nature energy

Article

https://doi.org/10.1038/s41560-025-01860-3

Solution-processed kesterite solar module with 10.1% certified efficiency

Received: 22 September 2024

Accepted: 7 August 2025

Published online: 15 September 2025

Check for updates

Chunxu Xiang[1,3], Mingjun Yuan[1,3], Chuan'an Ding[1], Yuanyuan Zheng[1], Yize Li[1], Xiaole Hu[2], Jie Zhang[2], Xinyu Li[1], Chengfeng Ma[1], Shaoying Wang[1] ✉, Weibo Yan[1], Chunlei Yang[2], Wei Huang[1] ✉ & Hao Xin[1] ✉

Solution processing has great advantages for emerging thin-film solar cells but remains a big challenge for multielemental inorganic films due to complicated phase evolution and grain growth during crystallization. Here we report the fabrication of uniform, large-area $Cu_2ZnSn(S,Se)_4$ (CZTSSe) films and solar modules from solution. By tuning the thiourea/metal ratio to increase film porosity—thereby promoting more uniform vertical reaction and lateral grain growth—we improved the uniformity of CZTSSe films and achieved a single-cell efficiency of 13.4% and a solar module efficiency of 8.91%. We further optimized the module structure to reduce non-ideal contact and patterning-induced shunt and resistive losses, resulting in a champion CZTSSe module with a National Renewable Energy Laboratory-certified efficiency of 10.1%. This module also exhibits the lowest cell-to-module loss in open circuit voltage and current density among state-of-the-art emerging thin-film solar modules. Our work demonstrates the viability of solution processing to deposit uniform, large-area CZTSSe film and efficient solar modules, advancing the development of the technology.

Photovoltaics (PV) play a pivotal role in transitioning towards a decarbonized society[1], which requires not only continued advancement of existing PV technologies[2] but also the development of green, cost-effective and sustainable solutions for new applications such as portable, flexible and semi-transparent PV[3–5]. Thin-film solar cells compatible with large-area, scalable solution processing have emerged at the forefront of next-generation PVs. Among them, perovskite and organic solar cells are developing rapidly, with laboratory efficiencies approaching that of crystalline silicon and exceeding 20%, respectively[6,7]. Kesterite-type $Cu_2ZnSn(S,Se)_4$ (CZTSSe), a counterpart semiconducting material of chalcopyrite-type $Cu(In,Ga)Se_2$ (CIGS)[8,9], is another emerging light-absorbing material for thin-film solar cells[10–12]. Besides environmentally benign elemental composition, high theoretical efficiency and superior stability, both CIGS[13] and CZTSSe[14–16] can be fabricated via solution processing. The combination of the superior properties of inorganic semiconducting materials and scalable solution processing might be the solution for green and low-cost PV technology.

However, the solution-based fabrication of multielemental inorganic materials differs markedly from that of perovskite-type or organic films[17,18], for which the target materials or constitutions either quickly developed during solvent evaporation or already exist in the solution. For CZTSSe or CIGS[19,20], it generally involves two steps: first, deposition of precursor film from solution by decomposing the chemicals (usually metal complexes) dissolved or formed in the solution, which is usually a mixture of several components, for example, $Cu_{1-x}S$, ZnS and SnS_2 for kesterite[21,22]; second, crystallization of precursor film in chalcogenide atmosphere to form the target material. The multiphase fusion reaction path generally produces an inhomogeneous film with high composition and electronic fluctuation due to a difference in thermal and dynamic reactivity of the secondary phases[23–26]. Recently, by using Cu^+–Sn^{4+} as

[1]State Key Laboratory of Flexible Electronics, Institute of Advanced Materials, Nanjing University of Posts and Telecommunications, Nanjing, China. [2]Center for Photonics Information and Energy Materials, Shenzhen Institute of Advanced Technology, Chinese Academy of Sciences, Shenzhen, China. [3]These authors contributed equally: Chunxu Xiang, Mingjun Yuan. ✉e-mail: iamshywang@njupt.edu.cn; vc@nwpu.edu.cn; iamhxin@njupt.edu.cn

the metal precursors (with thiourea (Tu) as S precursor) to control solution chemistry (equation (1)), the Xin group has successfully achieved almost pure kesterite precursor film (equation (2)), which undergoes a direct phase transformation reaction during selenization to form CZTSSe (equation (3)) without the secondary phases typically observed when using Cu^{+}–Sn^{2+} precursors[21,27].

$$\begin{aligned} &CuCl + Zn(OAc)_2 + SnCl_4 + Tu + DMSO \\ &\rightarrow Cu(Tu)_3Cl + Zn(Tu)_2(OAc)_2 + Sn(DMSO)_4Cl_4 \end{aligned} \quad (1)$$

$$Cu(Tu)_3Cl + Zn(Tu)_2(OAc)_2 + Sn(DMSO)_4Cl_4 \rightarrow Cu_2ZnSnS_4 \quad (2)$$

$$Cu_2ZnSnS_4 + Se \rightarrow Cu_2ZnSn(S,Se)_4 \quad (3)$$

The direct phase transformation reaction path leads to high-quality CZTSSe film[21,28] and a breakthrough in solar cell efficiency (13%)[29] after almost a decade stagnation at 12.6% (refs. 30,31). Fine control of film crystallization[22,32] and alloying[33,34] further pushes the efficiency to over 15% in the past 3 years[35], surpassing the benchmark for commercialization of this type of thin-film solar cell[36]. It is urgent to assess the scalability and suitability of solution processed inorganic absorber films for practical applications. In the previous work, we had fabricated a CZTSSe module with an efficiency of 4.3% (ref. 37). The low module efficiency and high cell-to-module (CTM) loss (56.81%)[37] reveal low absorber uniformity and non-ideal module fabrication.

In this work, we first identified that the poor uniformity of the CZTSSe film originates from uneven vertical crystallization caused by the rapid formation of a dense top layer that hinders selenium penetration. By increasing the content of Tu to produce a more porous film to allow sufficient Se penetration and more room for lateral grain growth, uniform CZTSSe film was achieved, leading to greatly improved single-cell performance and 8.91% efficiency solar module. We further modified the module structure to reduce non-ideal contact and scribing-induced shunting and series resistance, resulting in a champion module with a National Renewable Energy Laboratory (NREL)-certified efficiency of 10.1%.

Uniformity of solution-processed CZTSSe

The CZTSSe solar cells were fabricated from Cu^{+}–Sn^{4+}-based dimethyl sulfoxide (DMSO) precursor solution (Fig. 1a) by using simple compounds of CuCl, $Zn(OAc)_2$, $SnCl_4$ and Tu as the Cu, Zn, Sn and S precursors with a standard procedure according to a previous report[29]. We note that 10% Ag alloying was applied to CZTSSe, which was performed by substituting 10% CuCl with AgCl in the precursor solution. Ag alloying has been demonstrated to be an effective strategy to mitigate the band tailing and improve the device performance of kesterite solar cells[28,38,39] and has now become a standard for CZTSSe solar cells[15,16,22,29,32–34,40]. The precursor solution was deposited on Mo-coated soda lime glass (SLG) substrate to form the precursor film, which reacted with Se vapour (so called selenization) to form CZTSSe absorber film. The device was fabricated by subsequent deposition of a cadmium sulfide (CdS) buffer layer, intrinsic zinc oxide (ZnO) and indium-doped tin oxide (ITO) window layers and Ni/Al top contact grids. The configuration of the device is illustrated in Fig. 1b. The details of the preparation of the solution and device fabrication are given in the Methods.

To evaluate the film uniformity and reproducibility, solar cells were first fabricated from solution with the same composition as a previous report with Tu-to-total metal ion ratio of 1.5 (Tu/M = 1.5, denoted as Tu1.5)[29]. On one substrate with a dimension of 2.5 cm × 2.5 cm, 35 (5 column × 7 row) solar cell devices were fabricated (Supplementary Fig. 1). The statistical photovoltaic parameters of 140 cells (on 4 substrates) are shown in Supplementary Fig. 2 and Supplementary Table 1. The efficiency of the single cells is based on an active area of 0.1 cm^2. An average power conversion efficiency (PCE) of 12.39% was obtained with average open circuit voltage (V_{OC}) of 514.11 mV, fill factor (FF) of 69.16% and current density (J_{SC}) of 34.84 mA cm^{-2}, comparable to previous reports. The standard deviations for each parameter are somewhat large (0.29% for PCE, 1.03% for FF, 6.54 mV for V_{OC} and 0.84 mA cm^{-2} for J_{SC}), revealing relatively low film uniformity. As mentioned previously, the evolution of multielemental inorganic films differs markedly from that of perovskite or organic films; even with a direct phase transformation reaction path, the film morphology may change dramatically due to the relatively long crystallization duration and vertically uneven reactions, particularly given the much greater film thickness—typically in the micrometre range, as opposed to the hundreds of nanometres typical for organic and perovskite absorber films. To understand the origin of the non-uniformity, the crystallization process of CZTSSe film was monitored by interrupting the selenization. The top-view and cross-sectional scanning electron microscopy (SEM) images of the Tu1.5 precursor film and films at typical stages of the selenization are shown in Fig. 1c. The samples are labelled according to the selenization temperature, followed by the duration at that temperature. For example, 500 °C–5 min represents selenization at 500 °C for 5 min. More images of the grain growth are provided in Supplementary Fig. 3. It can be seen that, at the very early stage of the selenization (540 °C–0 min), a dense high crystalline top layer was already formed. As selenization progresses, crystallization occurs in the bottom layer alongside continued growth of the top grains, leading to the formation of a tri-layer structure with a poorly crystalline middle layer at 540 °C–10 min. However, as the selenization further progresses (540 °C, 15–25 min), only top grains coalesce without obvious changes in middle and bottom layers (Supplementary Fig. 3). This uneven vertical crystallization is the result of the dense top layer, which prohibits Se penetration. The depth profiles of Se at different stages of the selenization confirm this conclusion (Supplementary Fig. 4a). Further coalescence of the upper grains leads to uneven grain sizes and a rough surface (540 °C–20 min), which is more drastic for film 540 °C–25 min with a longer selenization time (Supplementary Fig. 3).

Based on the above analysis, improving the uniformity and surface flatness of the final absorber film requires a relatively porous top layer during the early stage of crystallization. This structure allows greater selenium diffusion into the film bulk, facilitating a more uniform reaction and providing space for lateral grain growth. Thus, we have increased the Tu/M ratio to 1.7 and fabricated CZTSSe absorber film and solar cells. SEM images (Fig. 1c and Supplementary Fig. 3) show that a more porous precursor film is indeed achieved due to decomposition of Tu during wet film thermal annealing, which produces a looser top crystalline layer at the early stage of selenization (540 °C–0 min) as expected, leading to the formation of uniform dense large-grain CZTSSe film with a flat surface (Fig. 1c, 540 °C–20 min, bottom). The depth profiles of Se at different stages of the selenization are shown in Supplementary Fig. 4b, which confirm a uniform vertical distribution of Se at all stages, attributed to the uniform and porous morphology of the precursor film.

The compositional uniformity of Tu1.5 and Tu1.7 films were further compared by time of flight-secondary ion mass spectrometer (TOF-SIMS) and energy-dispersive X-ray spectroscopy (EDS) line scans at different position of the films (Supplementary Figs. 5 and 6), which demonstrate that Tu1.7 has more uniform elemental composition both vertically and laterally. In addition, the morphological uniformity of the two films is also compared by measuring the grain sizes and their distributions at nine different locations, which shows that film Tu1.7 has a narrower grain size distribution (Supplementary Figs. 7 and 8). The high uniformity substantially improves solar cell performance, especially for V_{OC} and FF. From the statistical photovoltaic parameters of 140 Tu1.7 devices (Supplementary Fig. 2), an average PCE of 13.40% is achieved with an average V_{OC} of 535.69 mV, FF of 70.80% and J_{SC} of 35.33 mA cm^{-2}. The standard deviation of each parameter is reduced

https://doi.org/10.1038/s41560-025-01860-3

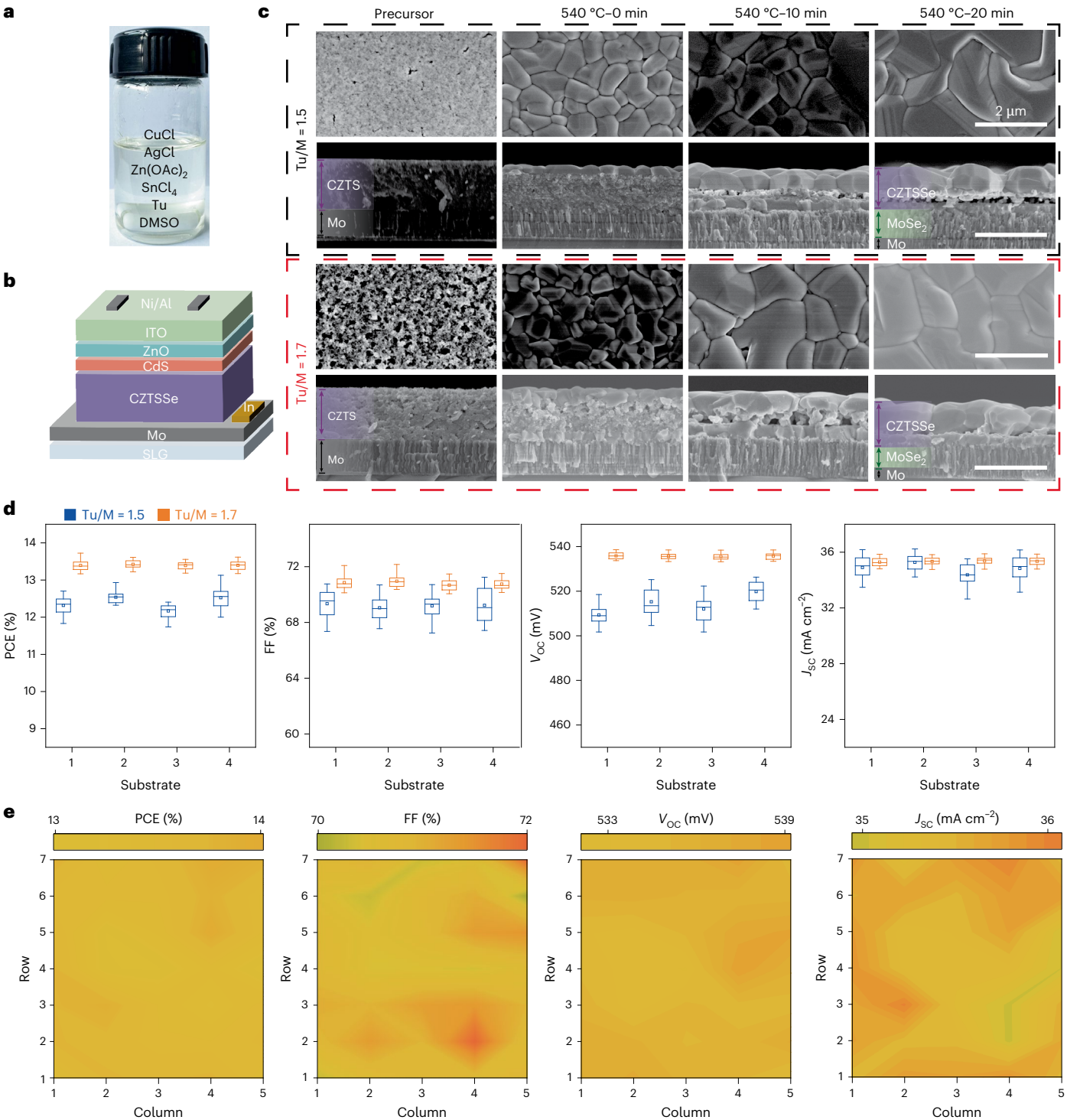

Fig. 1 | The uniformity of solution-processed kesterite solar cells. a, A picture of the precursor solution. **b**, An illustration of the kesterite solar cell with a configuration of SLG/Mo/CZTSSe/CdS/ZnO/ITO/Ni/Al. **c**, Top-view and cross-sectional SEM images of the precursor and absorber films with Tu/metal (M) ratio of 1.5 (Tu1.5) and 1.7 (Tu1.7) at different stages of the grain growth (selenization). **d**, Plots of the statistical photovoltaic parameters (PCE, FF, V_{OC}, and J_{SC}) of Tu1.5 and Tu1.7 solar cells. A total of 140 devices on 4 substrates (each contains 35 devices) fabricated in one batch are included for each condition. The box plots denote the median (centre line), mean value (dot) and 25th (bottom edge of the box), 75th (top edge of the box), 95th (upper whisker) and 5th (lower whisker) percentiles. **e**, Contour plots of the device parameter distribution of 35 cells on one substrate for Tu1.7.

to be only 0.13% for PCE, 0.39% for FF, 1.46 mV for V_{OC} and 0.28 mA cm^{-2} for J_{SC} (Supplementary Table 1).

The X-ray diffraction (XRD) data (Supplementary Fig. 9a) show that film Tu1.7 exhibits higher diffraction intensity than Tu1.5, confirming higher crystallinity. At the same time, the slight shift of Bragg peak positions to lower 2θ positions of Tu1.5 than Tu1.7 is in good agreement with overcrystallization or overselenization of film Tu1.5 at the late stage of the selenization. The representative current density–voltage (J–V) and external quantum efficiency (EQE) curves of the Tu1.5 and Tu1.7 solar cells are given in Supplementary Fig. 9b,c, demonstrating

https://doi.org/10.1038/s41560-025-01860-3

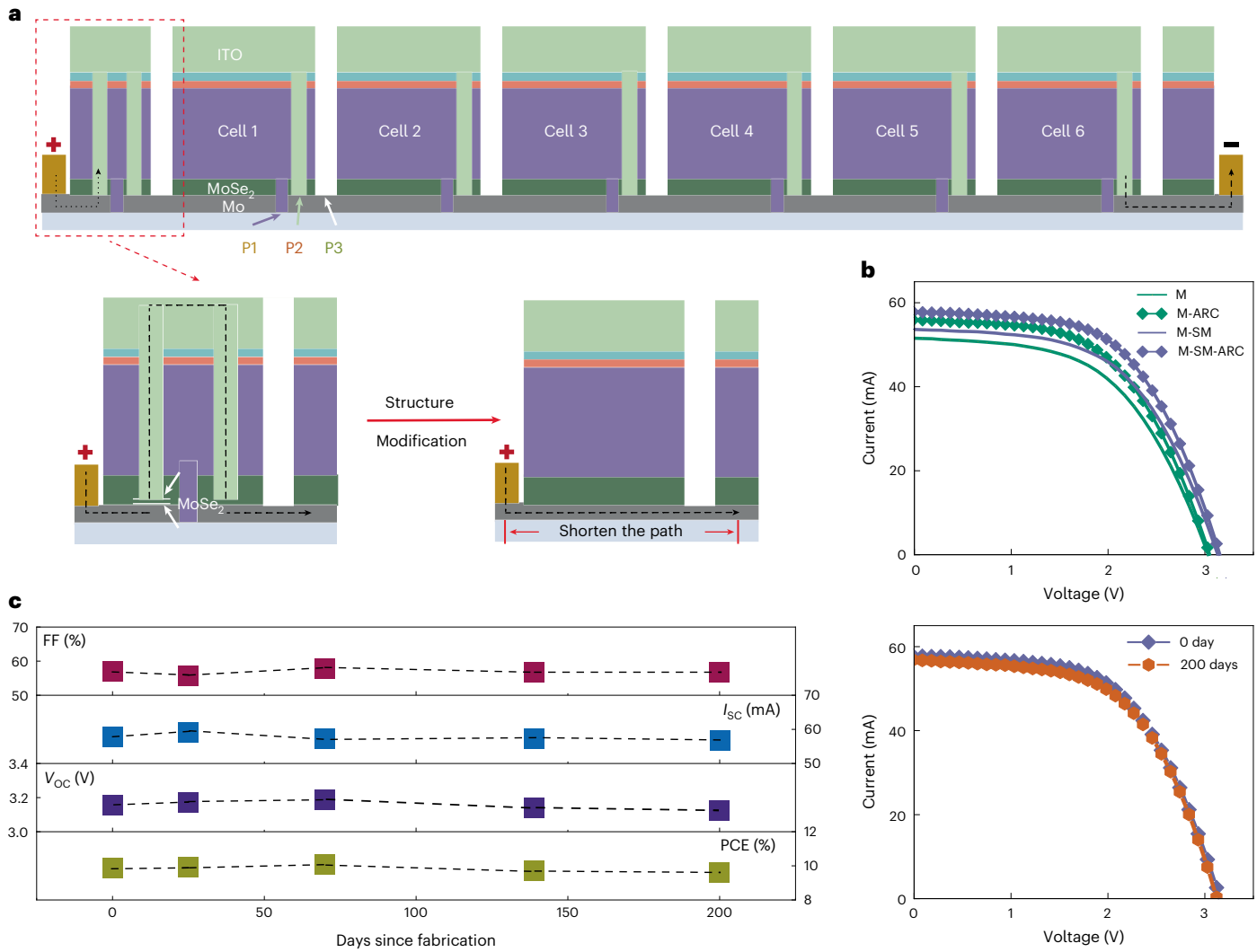

Fig. 2 | Kesterite solar module and stability. a, A cartoon of the module structure and structure modification. The dotted black line is the flow of the current. **b**, The *I*–*V* curves of the primary module without (M) and with antireflective coating (M-ARC), module after structure modification without (M-SM) and with ARC (M-SM-ARC). **c**, Module stability. The photovoltaic parameters of M-SM-ARC after storage in ambient air (temperature 25 °C, humidity 30–50% and indoor light) for different time (days) and the *I*–*V* curves measured at 0 day and 200 days. The dashed line serves as a guide to the eye.

a PCE of 12.72% for device Tu1.5 and 13.49% for device Tu1.7 with J_{SC}, V_{OC} and FF of 35.24 mA cm^{-2}, 0.536 V and 71.37%, respectively. The band gap extracted from the absorber edge of the EQE spectrum is 1.07 eV for Tu1.5 and 1.14 eV for Tu1.7 (Supplementary Fig. 9d), consistent with XRD data.

For a clear comparison of the uniformity between Tu1.5 and Tu1.7 absorber films, the statistical photovoltaic parameters from four sets of solar cells across four substrates are plotted side by side in Fig. 1d, clearly demonstrating higher uniformity in all parameters for the Tu1.7 devices. To further observe the homogeneity of Tu1.7 devices, the contour plots of the distribution of device parameters of all 35 pixels on one substrate is shown in Fig. 1e, with corresponding data for Tu1.5 plotted in Supplementary Fig. 10. The high uniformity of Tu1.7 devices clearly results from the porous precursor film, which promotes even grain growth. In addition, Supplementary Fig. 11 shows a cross-sectional SEM image of the Tu1.7 device. Except for the functional layers shown in Fig. 1b, a molybdenum selenide ($MoSe_2$) layer with a thickness about 800 nm can be clearly seen between Mo and CZTSSe, which was formed during selenization. The thin layer of $MoSe_2$ can facilitate Ohmic contact, thereby benefitting device performance, whereas an excessively thick $MoSe_2$ may create a barrier for charge transportation[41].

Module performance and stability

Based on the uniform CZTSSe absorber film, CZTSSe modules with standard structure were manufactured on 4 cm × 4 cm substrate with six subcells serially interconnected by three successive patterning steps, denoted P1, P2 and P3 (Fig. 2a). Details of the module fabrication are given in the Methods and Supplementary Fig. 12. The TOF-SIMS elemental depth profiles (Supplementary Fig. 13) and cross-sectional SEM images (Supplementary Figs. 14 and 15) at different positions of the module confirm that a uniform absorber film and other functional layers on top of it are achieved in large area. The cross-sectional SEM image of the finished module across the whole P1, P2 and P3 area (Supplementary Fig. 16) clearly demonstrates high flatness under the Tu1.7 condition. As observed before, some $MoSe_2$ remained at the bottom of P2 (Supplementary Fig. 16f), which may increase resistance to vertical charge transfer along the P2 channels. At the same time, the distance between P3 and P2 is approximately four times greater than that between P2 and P1 due to mechanical scribing, resulting in a larger dead area and increased CTM losses. Further optimization of the P3 patterning process is expected to reduce the dead zone and improve module efficiency.

The illumination area of the module is defined by a mask with a designed aperture area of 10.5 cm^2 (Supplementary Fig. 17).

https://doi.org/10.1038/s41560-025-01860-3

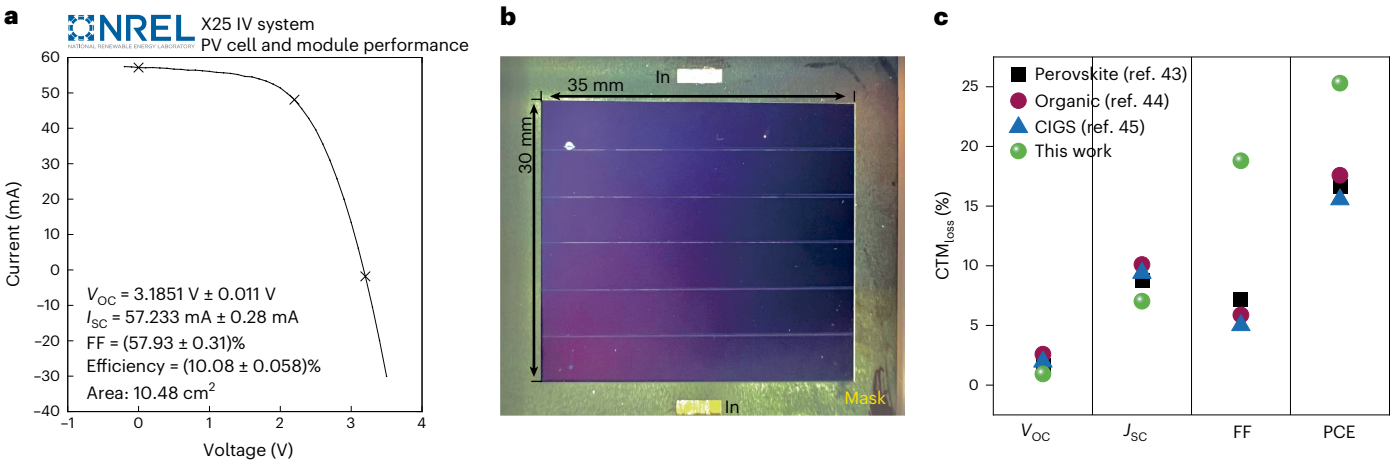

Fig. 3 | Certification of kesterite module and CTM losses. a, The *I*–*V* curve of the NREL-certified 10.08% efficient kesterite module. **b**, A picture of the obverse side of the certified module. The area is defined by the mask. **c**, A comparison of the CTM losses of the emerging thin-film solar modules (perovskite[43], organic[44] and CIGS[45]). NREL logo used with permission of the National Renewable Energy Laboratory.

The as-fabricated module (M) exhibits an efficiency of 7.95% with a current of 51.55 mA, a V_{OC} of 3.035 V and an FF of 53.33% (Fig. 2b and Supplementary Table 2). After applying an antireflective coating (ARC), the efficiency of the module (M-ARC) increased to 8.91% with current (I_{SC}), V_{OC} and FF of 55.88 mA, 3.048 V and 54.89%, respectively (Fig. 2b and Supplementary Table 2). For a clear comparison, the device parameters of the single cell and the module (V_{OC} is distributed to six subcells) are summarized in Supplementary Table 2. It can be clearly seen that the primary CTM loss is FF. Obviously, the low FF comes from low shunt resistance (R_{Sh}) and high series (R_S), which are 343 Ω cm^2 and 4.54 Ω cm^2 for the module M and 12,662 Ω cm^2 and 1.74 Ω cm^2 for the single cell. One reason for the high R_S is the low conductivity of the ITO (typically 50 Ω/□ in our laboratory), which reduces the device FF by 9.8% when the area of the single cell is increased from 0.107 cm^2 to 1.019 cm^2 (ref. 29). Another reason is that the subcell of the module is much wider than the single cell, which increases the lateral transport distance and causes higher series resistance. The thicker CZTSSe absorber film compared with organic photovoltaics and perovskites results in a longer P2 channel, leading to higher resistance. This issue could be solved by optimization of the ITO layer as well as putting on top metal grid lines in the future work[42].

Another reason for the low FF is the $MoSe_2$ layer between Mo and CZTSSe as discussed earlier, which creates extra resistance compared with organic and perovskite solar cells. To minimize the effects of ITO and $MoSe_2$, the module structure near the anode is redesigned (Fig. 2a). After structure modification (SM), the number of scribing is reduced from 7 to 6 for P1 and 8 to 6 for P2, which shortens the path of the current along the ITO channel as well as across the $MoSe_2$ layer. This leads to a notable reduction in R_S from 4.54 to 3.98 Ω cm^2 in module M-SM, which contributes to an improved FF (55.22%) and module efficiency of 8.84% (Fig. 2b and Supplementary Table 2). After applying the ARC, the champion module (M-SM-ARC) achieved a home-measured PCE of 9.88% with I_{SC} of 57.78 mA, V_{OC} of 3.155 V and FF of 56.90% (Fig. 2b and Supplementary Table 2). We note that ARC not only improves module J_{SC} but also enhances V_{OC} and FF of all modules. This could be explained by the good coverage of the P3 grooves, which reduces the R_S and R_{Sh} resistance caused by non-ideal mechanical scribing. The combination of SM and ARC results in improvements of 12.1% in I_{SC}, 4.0% in V_{OC} and 6.7% in FF. Importantly, the kesterite solar module maintains over 98% of its original efficiency after being stored in ambient air for 200 days without any encapsulation, demonstrating high stability and suitability for practical applications (Fig. 2c).

Champion module and CTM loss

Module M-SM-ARC was sent to NREL for evaluation, which demonstrates a certified PCE of 10.08% with V_{OC} of 3.185 V, I_{SC} of 57.23 mA and FF of 57.93% (Fig. 3a). The aperture area of the mask was measured to be 10.48 cm^2 by NREL. The discrepancy, where the home-measured efficiency is lower than the certified value, may be caused by non-ideally uniform illumination from our solar simulator. Figure 3b depicts the obverse side of the certified module. More details of the NREL certification are provided in Supplementary Figs. 18–20. The bandgap (E_g) of the CZTSSe module absorber, calculated to be 1.14 eV from the EQE measured by NREL (Supplementary Fig. 20), is the same as that of the single cell (E_g = 1.14 eV; Supplementary Fig. 9d).

The CTM losses of the champion CZTSSe module as well as perovskite, organic and vacuum-based CIGS thin-film modules are calculated according to the reported methods, and the results are summarized in Fig. 3c and Supplementary Table 3. The references of perovskite[43], organic[44] and CIGS[45] are selected from the latest publications from the same research groups that hold the current record efficienies, as listed in Martin A. Green's 'Solar Cell Efficiency Tables (Version 64)'[35]. The remarkable low CTM$_{V_{OC}}$ loss (only 0.93%) indicates the difference in defect-assisted recombination between the single cell and the module can be negligible. For the 7.03% CTM$_{J_{SC}}$ loss, 5.01% comes from the dead zone resulting from the patterning of the module (Supplementary Fig. 17) and the remaining 2.02% can be attributed to the fact that the current adjusts to the subcell with the lowest current in the module. The CTM$_{V_{OC}}$ and CTM$_{J_{SC}}$ losses of the CZTSSe module are the lowest among the four thin-film modules, which are the results of the high uniformity of the solution-processed CZTSSe absorber film, benefitted from the well-controlled reaction path and grain growth through solution chemistry regulation. The biggest loss of the current CZTSSe module comes from CTM$_{FF}$ (18.8%), almost three times higher than that of perovskite (7.19%), organic (5.87%) and CIGS (5.01%). As discussed earlier, the large CTM$_{FF}$ mainly originated from the poor conductivity of the ITO and the extra resistance and shunting due to non-ideal patterning and contact. The CTM losses were further analysed by modelling the *J*–*V* curves of the single cell and the module using SOLEY (Methods), and the results are shown in Supplementary Fig. 21. The simulation shows that the resistance accounts for 0.19% CTM$_{V_{OC}}$ and 0.34% CTM$_{J_{SC}}$ losses but as high as 19.27% CTM$_{FF}$ loss, confirming that modularization-induced losses primarily occur through resistive effects. The results also illustrate the resilience of the kesterite fabrication process, which maintains excellent performance even during upscaling. The high resistance can be solved by

optimization of the module fabrication process. The efficiency of the module can thus practically exceed 13% by reducing CTM_{FF} losses based on the current record efficiency of 15.1% and is expected to exceed 15% in the near future based on the fast development of this type of thin-film technology.

Conclusion

We demonstrate a certified 10.1% (10.48 cm^2) efficiency kesterite CZTSSe solar module from solution by controlling crystallization to improve film uniformity and modifying module structure to reduce charge transport resistance. Characterizations show that the poor uniformity of the CZTSSe film fabricated under reference condition (Tu1.5) originated from quick formation of a dense crystalline top layer at the early stage of the selenization, which prohibits penetration of Se and leads to uneven vertical crystallization. Increasing the content of Tu in the solution (Tu1.7) produces a more porous precursor film, which results in a looser top layer that allows sufficient penetration of Se into film bulk and more room for lateral grain growth, leading to greatly improved film uniformity and surface flatness. This strategy improves the average efficiency of single cells from 12.39% to 13.40%, while reducing the standard deviation from 0.29% to 0.13%. The excellent morphological and compositional uniformity is maintained with upscaling, achieving 8.91% efficient solar module. Furthermore, structure modification shortens the path of the current along the low conductive ITO channel and resistive $MoSe_2$ layer, leading to greatly improved FF and module efficiency. The champion CZTSSe module demonstrates the lowest $CTM_{V_{OC}}$ and $CTM_{J_{SC}}$ losses among state-of-the-art emerging thin-film solar modules and high stability with efficiency maintained over 98% after 200 days of air exposure without encapsulation. The current module is still limited by high resistance, resulting in a substantial CTM_{FF} loss (18.8%); much higher efficiency can be expected with further optimization of the module fabrication process. Our results demonstrate the practical prospects of solution-processed inorganic semiconducting materials for application in thin-film PV and other related optoelectronic devices.

Methods

Preparation of the kesterite precursor solutions

The precursors used for making the precursor solutions are AgCl (Aladdin), CuCl (Aladdin), $Zn(OAc)_2$ (99.99%, Aladdin), $SnCl_4$ (99%, J&K) and Tu. The mole ratios of Ag/(Ag+Cu), (Cu+Ag)/(Zn+Sn) and Zn/Sn were fixed at 0.1, 0.75 and 1.15, respectively. The mole ratio of Tu/(Cu+Ag+Zn+Sn) was 1.5 for solution Tu1.5 and 1.7 for solution Tu1.7. In addition, NaCl (with Na/Cu of 0.01) was added to the solution. The precursor solutions were prepared in a glove box at room temperature with controlled O_2 and H_2O levels below 5 ppm. For solution Tu1.5, first, Ag–Cu–Tu–DMSO solution was made by dissolving 1.71 g Tu (after twice recrystallization) in 4 ml DMSO (99.8%, Aladdin) in vial #1 followed by sequentially adding 0.092 g AgCl, 0.575 g CuCl and 3.7 mg NaCl under stirring until clear. Second, Sn–Zn–DMSO solution was made by adding 1.042 g $SnCl_4$ to vial #2 and sealed, followed by injection of 4 ml DMSO into the vial using a syringe, resulting in a suspension; then, 0.844 g $Zn(OAc)_2$ was added into the suspension under stirring until clear. Vial #1 solution was mixed with vial #2 solution to produce a pale-yellow precursor solution. Solution Tu1.7 was similarly prepared by adding extra Tu.

Fabrication of single-junction solar cells

The dimension of Mo-coated SLG substrates was 2.5 cm × 2.5 cm for single cells and 4 cm × 4 cm for modules. First, the Mo-coated SLG substrates were placed on a polytetrafluoroethylene rack and immersed in a beaker containing ethanol for 15 min of ultrasonic cleaning at 40 °C, followed by ultrasonic cleaning in ultrapure water for the same time. The substrates were dried with a N_2 flow before use. The precursor solution was filtered through a 0.8-μm polytetrafluoroethylene filter and then spin-coated onto the cleaned Mo-coated SLG substrates at a spin speed of 2,000 rpm for 20 s. The thickness of the Mo layer is about 800–1,000 nm. The wet films were immediately annealed on a hot plate at 340 °C for 90 s. The coating–annealing–cooling cycle was performed seven times to create a 2-μm-thick precursor film. The precursor film was then placed in a 6 cm × 6 cm × 1 cm graphite box with 500-mg Se tablets. The lid of the graphite box has five 1-mm holes, one in the middle and the others near the four corners. The graphite box was put into a Rapid Heating tube furnace for selenization. The tube was evacuated until the pressure reached 5×10^{-2} torr and then refilled with argon to atmospheric pressure. The evacuation and refilling process was repeated three times to remove water and oxygen from the tube. The tube was heated up at a rate of 2 °C s^{-1} from 25 °C to 540 °C and maintained at 540 °C for 20 min. Then, the furnace (samples) was cooled down naturally to room temperature. After selenization, the films were submerged in ultrapure water (~18.2 MΩ cm) and then transferred into a beaker in 65 °C water bath with 220 mL aqueous solution containing 3.3 mmol $CdSO_4$, 0.0165 mmol Tu and 28 ml NH_4OH (~25–28%) for chemical bath deposition of CdS buffer layer. The chemical bath deposition was performed for 12 min under stirring to deposit ~40 nm CdS. The CZTSSe/CdS samples underwent heterojunction annealing on a hot plate in a N_2-filled glove box. The annealing temperature was 110 °C, for 12 h. For single cells, the window layer of 50-nm i-ZnO and 150-nm ITO were deposited by radiofrequency sputtering at room temperature, followed by deposition of top contact grids of 50-nm Ni and 500-nm Al by thermal deposition through shadow masks. The device area was defined by mechanical scribing. For modules, the ITO layer was 330 nm and no top contact grids were used.

Fabrication of solar modules

P1 and P2 patterning were scribed by using a 532-nm picosecond laser with a power of 3 W and a frequency of 100 kHz at a motion speed of 20 mm s^{-1}. The output power of the laser used for P1 was 80–85% (2.5 W), and each line (pattern) was scribed only once. The depth of the line was about 1 μm, and Mo was precisely removed. The output power of the laser used for P2 was 30% (0.9 W), and four lines were scribed for each pattern with an interval of 10 μm. To completely remove the possible residues, the four lines were further cleaned by the same laser with output power of 21% (0.63 W). These eight lines were close enough to integrate into one wider groove with most of the $MoSe_2$/CZTSSe/CdS/i-ZnO layers removed. For P3 patterning, a razor blade was used to scribe out a line (removing $MoSe_2$/CZTSSe/CdS/i-ZnO/ITO) on the side of P2 to separate the top electrodes of the adjacent cells.

Film and device characterizations

The morphology of the absorber films was measured on a Hitachi S4800 scanning electron microscope. The elemental distribution along the depth of the absorber and the device was characterized using SEM–EDS (Oxford Xplore30) line scanning and a time of flight-secondary ion mass spectrometer. The TOF-SIMS analysis was conducted using Bi^{3+} as a primary ion source with an energy of 30 keV and a current at picoampere (pA) level. The analysis area was 50 × 50 μm^2. During the sputtering process, Cs^+ is selected as the sputtering ion with an energy of 1 keV and a current at the nanoampere (nA) level. The sputtering area was 200 × 200 μm^2. The current density–voltage (J–V) curves of the solar cells were measured using Keithley 2400 Source Meter under simulated AM 1.5 sunlight at 100 mW cm^{-2} irradiance generated by a AAA sun simulator (CROWNTECH). The light intensity was calibrated by a calibrated Si reference cell. The J–V measurement was performed in air at a temperature of around 300 K and humidity of about 40%. The EQE spectra of the solar cells were measured on Enlitech QE-R3018 using calibrated Si and Ge diodes (Enli Technology) as references. The aforementioned solar simulation system and Keithley 2400 Source Meter were used to collect the current–voltage (I–V) data.

Calculation of the CTM losses

According to the calculation method of the literature[46–48], the CTM losses of the photovoltaic performance parameters of internal series-connected type modules can be calculated via

$$\mathrm{CTM_{PCE}} = 1 - \mathrm{PCE_M}/\mathrm{PCE_C}$$

$$\mathrm{CTM}_{V_{OC}} = 1 - \frac{V_{OC_M}}{n \times V_{OC_C}}$$

$$\mathrm{CTM}_{J_{SC}} = 1 - \frac{J_{SC_M}}{J_{SC_C}} = 1 - n \times \frac{S_C \times I_{SC_M}}{I_{SC_C} \times S_M}$$

$$\mathrm{CTM_{FF}} = 1 - \mathrm{FF_M}/\mathrm{FF_C}.$$

The CTM losses of PCE, V_{OC}, J_{SC} and FF are denoted by $\mathrm{CTM_{PCE}}$, $\mathrm{CTM}_{V_{OC}}$, $\mathrm{CTM}_{J_{SC}}$ and $\mathrm{CTM_{FF}}$. The subscripts M and C denote the modules and the single cells, respectively.

Simulation of CTM losses

The CTM losses were modelled using SOLEY, which is a new simulation tool developed at the Universitat Politècnica de Catalunya by Zacharie Victor Samuel Nathana Jehl for thin-film solar cell modelling. The single cell is modelled with a recombination parameter J_0 of 4.9×10^{-6} mA cm^{-2}, a diode ideality factor n of 1.3, an R_S of 1 Ω cm^2 and an R_{Sh} of 1×10^4 Ω cm^2. The J_0 and n are the same as the values extracted from the measured J–V data of the single cell, while the R_S and R_{Sh} are very close to the extracted values, which are respectively 1.74 Ω cm^2 and 1.27×10^4 Ω cm^2. The module was simulated with the same J_0 and n as those of the single cells, with the R_S and R_{Sh} values respectively adjusted to 3.5 Ω cm^2 and 1×10^3 Ω cm^2.

Reporting summary

Further information on research design is available in the Nature Portfolio Reporting Summary linked to this article.

Data availability

The data that support the findings of this study are available within the article and its Supplementary Information. Source data are provided with this paper.

Code availability

The simulation tool called SOLEY was developed at the Universitat Politècnica de Catalunya by Zacharie Victor Samuel Nathana Jehl for thin-film solar cell modelling. It was used as a supporting tool for simulating the J–V curves and CTM losses. The code is proprietary.

References

1. Lennan, M. & Morgera, E. The Glasgow Climate Conference (COP26). *Int. J. Mar. Coast. Law* **37**, 137–151 (2022).
2. Polman, A. et al. Photovoltaic materials: present efficiencies and future challenges. *Science* **352**, aad4424 (2016).
3. Hashemi, S. A., Ramakrishna, S. & Aberle, A. G. Recent progress in flexible-wearable solar cells for self-powered electronic devices. *Energy Environ. Sci.* **13**, 685–743 (2020).
4. Holzhey, P. et al. Toward commercialization with lightweight, flexible perovskite solar cells for residential photovoltaics. *Joule* **7**, 257–271 (2023).
5. Bing, J. et al. Total equivalent energy efficiency metric for building-integrated photovoltaic windows. *Joule* **7**, 2668–2683 (2023).
6. Fu, J. et al. 19.31% binary organic solar cell and low non-radiative recombination enabled by non-monotonic intermediate state transition. *Nat. Commun.* **14**, 1760 (2023).
7. Gao, H. et al. Homogeneous crystallization and buried interface passivation for perovskite tandem solar modules. *Science* **383**, 855–859 (2024).
8. Chen, S. et al. Electronic structure and stability of quaternary chalcogenide semiconductors derived from cation cross-substitution of II-VI and I-III-VI$_2$ compounds. *Phys. Rev. B* **79**, 165211 (2009).
9. Mitzi, D. B. et al. The path towards a high-performance solution-processed kesterite solar cell. *Sol. Energy Mater. Sol. Cells* **95**, 1421–1436 (2011).
10. Liu, X. et al. The current status and future prospects of kesterite solar cells: a brief review. *Prog. Photovolt.* **24**, 879–898 (2016).
11. Giraldo, S. et al. Progress and perspectives of thin film kesterite photovoltaic technology: a critical review. *Adv. Mater.* **31**, 1806692 (2019).
12. Liu, F. et al. Emerging inorganic compound thin film photovoltaic materials: progress, challenges and strategies. *Mater. Today* **41**, 120–142 (2020).
13. Zhang, T. et al. High efficiency solution-processed thin-film Cu(In,Ga)(Se,S)$_2$ solar cells. *Energy Environ. Sci.* **9**, 3674–3681 (2016).
14. Deng, H. et al. Novel symmetrical bifacial flexible CZTSSe thin film solar cells for indoor photovoltaic applications. *Nat. Commun.* **12**, 3107 (2021).
15. Yu, Z. et al. Unveiling the selenization reaction mechanisms in ambient air-processed highly efficient kesterite solar cells. *Adv. Energy Mater.* **13**, 2300521 (2023).
16. Li, Y. et al. Suppressing element inhomogeneity enables 14.9% efficiency CZTSSe solar cells. *Adv. Mater.* **36**, 2400138 (2024).
17. Shamsi, J. et al. Metal halide perovskite nanocrystals: synthesis, post-synthesis modifications, and their optical properties. *Chem. Rev.* **119**, 3296–3348 (2019).
18. Bronstein, H. et al. The role of chemical design in the performance of organic semiconductors. *Nat. Rev. Chem.* **4**, 66–77 (2020).
19. Jiang, J. et al. Highly efficient copper-rich chalcopyrite solar cells from DMF molecular solution. *Nano Energy* **69**, 104438 (2020).
20. Yu, S. et al. Solution-processed chalcopyrite solar cells: the grain growth mechanism and the effects of Cu/In mole ratio. *Adv. Energy Mater.* **12**, 2103644 (2021).
21. Gong, Y. et al. Identifying the origin of the V_{OC} deficit of kesterite solar cells from the two grain growth mechanisms induced by Sn^{2+} and Sn^{4+} precursors in DMSO solution. *Energy Environ. Sci.* **14**, 2369–2380 (2021).
22. Zhou, J. et al. Control of the phase evolution of kesterite by tuning of the selenium partial pressure for solar cells with 13.8% certified efficiency. *Nat. Energy* **8**, 526–535 (2023).
23. Xin, H. et al. 8% efficient Cu$_2$ZnSn(S,Se)$_4$ solar cells from redox equilibrated simple precursors in DMSO. *Adv. Energy Mater.* **4**, 1301823 (2014).
24. Martinho, F. et al. Persistent double-layer formation in kesterite solar cells: a critical review. *ACS Appl. Mater. Interfaces* **12**, 39405–39424 (2020).
25. Cui, Y. et al. DMF-based large-grain spanning Cu$_2$ZnSn(S$_x$,Se$_{1-x}$)$_4$ device with a PCE of 11.76. *Adv. Sci.* **9**, 2201241 (2022).
26. Zhang, X. et al. Suppressed interface defects by GeSe$_2$ post-deposition treatment enables high-efficiency kesterite solar cells. *Adv. Funct. Mater.* **33**, 2211315 (2023).
27. Gong, Y. et al. Sn^{4+} precursor enables 12.4% efficient kesterite solar cell from DMSO solution with open circuit voltage deficit below 0.30 V. *Sci. China Mater.* **64**, 52–60 (2020).
28. Gong, Y. et al. Ag incorporation with controlled grain growth enables 12.5% efficient kesterite solar cell with open circuit voltage reached 64.2% Shockley–Queisser limit. *Adv. Funct. Mater.* **31**, 2101927 (2021).

29. Gong, Y. et al. Elemental de-mixing-induced epitaxial kesterite/CdS interface enabling 13%-efficiency kesterite solar cells. *Nat. Energy* **7**, 966–977 (2022).
30. Wang, W. et al. Device characteristics of CZTSSe thin-film solar cells with 12.6% efficiency. *Adv. Energy Mater.* **4**, 1301465 (2013).
31. Son, D.-H. et al. Effect of solid-H_2S gas reactions on CZTSSe thin film growth and photovoltaic properties of a 12.62% efficiency device. *J. Mater. Chem. A* **7**, 25279–25289 (2019).
32. Xu, X. et al. Controlling selenization equilibrium enables high-quality kesterite absorbers for efficient solar cells. *Nat. Commun.* **14**, 6650 (2023).
33. Wang, J. et al. Ge bidirectional diffusion to simultaneously engineer back interface and bulk defects in the absorber for efficient CZTSSe solar cells. *Adv. Mater.* **34**, 2202858 (2022).
34. Shi, J. et al. Multinary alloying for facilitated cation exchange and suppressed defect formation in kesterite solar cells with above 14% certified efficiency. *Nat. Energy* https://doi.org/10.1038/s41560-024-01551-5 (2024).
35. Green, M. A. et al. Solar cell efficiency tables (Version 64). *Prog. Photovolt. Res. Appl.* **32**, 425–441 (2024).
36. Wang, A. et al. Analysis of manufacturing cost and market niches for Cu_2ZnSnS_4 (CZTS) solar cells. *Sustain. Energy Fuels* **5**, 1044–1058 (2021).
37. Yuan, M. et al. 4.3% efficient kesterite solar cell modules. *Sci. Bull.* **68**, 1497–1499 (2023).
38. Yuan, Z. K. et al. Engineering solar cell absorbers by exploring the band alignment and defect disparity: the case of Cu- and Ag-based kesterite compounds. *Adv. Funct. Mater.* **25**, 6733–6743 (2015).
39. Qi, Y. et al. Engineering of interface band bending and defects elimination via Ag-graded active layer for efficient $(Cu,Ag)_2ZnSn(S,Se)_4$ solar cells. *Energy Environ. Sci.* **10**, 2401–2410 (2017).
40. Zhou, Y. et al. 11.4% efficiency kesterite solar cells on transparent electrode. *Adv. Energy Mater.* **13**, 2300253 (2023).
41. Li, J. et al. A temporary barrier effect of the alloy layer during selenization: tailoring the thickness of $MoSe_2$ for efficient $Cu_2ZnSnSe_4$ solar cells. *Adv. Energy Mater.* **5**, 1402178 (2015).
42. Bermudez, V. & Perez-Rodriguez, A. Understanding the cell-to-module efficiency gap in $Cu(In,Ga)(S,Se)_2$ photovoltaics scale-up. *Nat. Energy* **3**, 466–475 (2018).
43. Zhang, W. et al. Dual-site synergistic passivation for highly efficient and stable perovskite solar cells. *Adv. Energy Mater.* **12**, 2202189 (2022).
44. Fan, J. Y. et al. High-performance organic solar modules via bilayer-merged-annealing assisted blade coating. *Adv. Mater.* **34**, 2110569 (2022).
45. Kato, T. $Cu(In,Ga)(Se,S)_2$ solar cell research in Solar Frontier: progress and current status. *Jpn J. Appl. Phys.* **56**, 04CA02 (2017).
46. Hanifi, H. et al. A practical optical and electrical model to estimate the power losses and quantification of different heat sources in silicon based PV modules. *Renew. Energy* **127**, 602–612 (2018).
47. Haschke, J. et al. Silicon heterojunction solar cells: recent technological development and practical aspects-from lab to industry. *Sol. Energy Mater. Sol. Cells* **187**, 140–153 (2018).
48. Yang, J. Y. et al. Research on decrease of cell to module loss for crystalline silicon photovoltaic module. *J. Renew. Sustain. Energy* **5**, 052003 (2013).

Acknowledgements

H.X. and W.Y. acknowledge the funding from the National Key Research and Development Program of China (grant nos. 2024YFB4205001 and 2019YFE0118100). S.W. acknowledges the funding from the National Key Research and Development Program of China (grant no. 2024YFB4205004). H.X. and W.Y. acknowledge the funding from the Major Basic Research Projects of the Shandong Natural Science Foundation (grant no. ZR2021ZD25). H.X. acknowledges the funding from National Natural Science Foundation of China (grant no. 22075150). C.X. acknowledges the support of Postgraduate Research & Practice Innovation Program of Jiangsu Province (grant no. KYCX23_0978). We thank Z. V. S. N. Jehl from the Universitat Politècnica de Catalunya for CTM losses modelling and valuable discussions.

Author contributions

H.X. directed the overall project. H.X., C.X. and M.Y. conceived the idea and designed the project. H.X. and C.X. co-wrote the paper. C.X. fabricated the single-cells and modules, and performed material and device characterizations. M.Y. designed module structure modification and assisted module fabrication. C.D. and X.H. provided assistance in module patterning. Y.Z. and Y.L participated in single-cell fabrication, optimization and data collection. X.L., C.M. and W.Y. provided assistance in XRD, SEM, *J–V* and EQE analysis. S.W. designed SEM–EDS and TOF-SIMS experiments and co-revised paper. J.Z. and C.Y. provided guidance on module preparation. W.H. provided financial assistance. All authors read and commented on the paper.

Competing interests

The authors declare no competing interests.

Additional information

Supplementary information The online version contains supplementary material available at https://doi.org/10.1038/s41560-025-01860-3.

Correspondence and requests for materials should be addressed to Shaoying Wang, Wei Huang or Hao Xin.

Peer review information *Nature Energy* thanks Stela Canulescu, Dae-Hwan Kim, Susan Schorr and the other, anonymous, reviewer(s) for their contribution to the peer review of this work.

nature portfolio

Corresponding author(s): Hao Xin

Solar Cells Reporting Summary

Nature Portfolio wishes to improve the reproducibility of the work that we publish. This form is intended for publication with all accepted papers reporting the characterization of photovoltaic devices and provides structure for consistency and transparency in reporting. Some list items might not apply to an individual manuscript, but all fields must be completed for clarity.

For further information on Nature Research policies, including our data availability policy, see Authors & Referees.

Experimental design

Please check the following details are reported in the manuscript, and provide a brief description or explanation where applicable.

1. Dimensions

Area of the tested solar cells	☒ Yes	The area is 0.1 cm2 for single cell devices and 10.48 cm2 for modules.
	☐ No	*Explain why this information is not reported/not relevant.*
Method used to determine the device area	☒ Yes	The area of module is defined by a mask and measured by National Renewable Energy Laboratory (NREL) .
	☐ No	

2. Current-voltage characterization

Current density-voltage (J-V) plots in both forward and backward direction	☐ Yes	Only forward direction is provided because there is no difference for kesterite solar cells in forward and backward scan.
	☒ No	
Voltage scan conditions	☒ Yes	Scanned from -0.2 V to 0.6 V with a step of 20 mV for single cell devices and from -0.2 V to 3.5 V with a step of 95 mV for modules without dwell time.
	☐ No	*Explain why this information is not reported/not relevant.*
Test environment	☒ Yes	The certified module was tested in NREL under standard condition and other devices were measured at room temperature in ambient air.
	☐ No	*Explain why this information is not reported/not relevant.*
Protocol for preconditioning of the device before its characterization	☐ Yes	*Provide a description of the protocol.*
	☒ No	No preconditioning was applied.
Stability of the J-V characteristic	☐ Yes	*Provide a description of the method used. The stability of the J-V characteristic can be verified with time evolution of the maximum power point or with the photocurrent at maximum power point; see ref. 5 for details.*
	☒ No	Kesterite solar cells are very stable and no need for this measurement.

3. Hysteresis or any other unusual behaviour

Description of the unusual behaviour observed during the characterization	☐ Yes	*Provide a description of hysteresis or any other unusual behaviour observed during the characterization.*
	☒ No	No hysteresis and other unusual behavior were observed.
Related experimental data	☐ Yes	*Provide a description of the related experimental data.*
	☒ No	No hysteresis and other unusual behavior were observed.

4. Efficiency

External quantum efficiency (EQE) or incident photons to current efficiency (IPCE)	☒ Yes	EQEs are provided in Supplementary Fig. 9c and Supplementary Fig. 20.
	☐ No	*Explain why this information is not reported/not relevant.*
A comparison between the integrated response under the standard reference spectrum and the response measure under the simulator	☒ Yes	Fig. 2b and Fig. 3a, Supplementary Fig. 9c and Supplementary Fig. 20a.
	☐ No	*Explain why this information is not reported/not relevant.*

For tandem solar cells, the bias illumination and bias voltage used for each subcell

☐ Yes
☒ No

Provide a description of the measurement conditions.

N/A

5. Calibration

Light source and reference cell or sensor used for the characterization

☒ Yes
☐ No

The intensity of the light source was calibrated by a standard silicon solar cell certified by NREL.

Explain why this information is not reported/not relevant.

Confirmation that the reference cell was calibrated and certified

☒ Yes
☐ No

The reference cell was certified by NREL.

Explain why this information is not reported/not relevant.

Calculation of spectral mismatch between the reference cell and the devices under test

☒ Yes
☐ No

Spectral mismatch were calculated by the certification agencies (NREL).

Explain why this information is not reported/not relevant.

6. Mask/aperture

Size of the mask/aperture used during testing

☒ Yes
☐ No

A mask with an area of 10.48 cm2 was used for modules.

Explain why this information is not reported/not relevant.

Variation of the measured short-circuit current density with the mask/aperture area

☐ Yes
☒ No

Report the difference in the short-circuit current density values measured with the mask and aperture area.

Modules were only measured device with the mask.

7. Performance certification

Identity of the independent certification laboratory that confirmed the photovoltaic performance

☒ Yes
☐ No

The certification laboratory is NREL for the module.

Explain why this information is not reported/not relevant.

A copy of any certificate(s)

☒ Yes
☐ No

Supplementary Fig. 19 and Supplementary Fig. 20.

Explain why this information is not reported/not relevant.

8. Statistics

Number of solar cells tested

☒ Yes
☐ No

140 for each condition.

Explain why this information is not reported/not relevant.

Statistical analysis of the device performance

☒ Yes
☐ No

Given in the figure captions of Fig. 1d and Supplementary. Fig. 2.

Explain why this information is not reported/not relevant.

9. Long-term stability analysis

Type of analysis, bias conditions and environmental conditions

☒ Yes
☐ No

Fig. 2c. Long-term stability, stored in ambient air without encapsulation.

Explain why this information is not reported/not relevant.